



Corrosion behaviors and mechanism of $\text{Al}_x\text{CrFeMnCu}$ high-entropy alloys in a 3.5 wt% NaCl solution

Li Feng ^{a,b,*}, Yang Yang ^a, Yanchun Zhao ^{a,b}, Kai Ma ^a, Junpeng Cui ^a

^a School of Material Science and Technology, Lanzhou University of Technology, Lanzhou 730050, China

^b State Key Laboratory of Advanced Processing and Recycling of Nonferrous Metals, Lanzhou University of Technology, Lanzhou 730050, China



ARTICLE INFO

Keywords:

High-entropy alloys
Microstructure
Corrosion behavior
Passive film
XPS

ABSTRACT

This study investigated the corrosion behavior of as-cast $\text{Al}_x\text{CrFeMnCu}$ ($x = 0, 0.5, 1.0, 1.5, 2.0$) high-entropy alloys (HEAs) in a 3.5 wt% NaCl solution at room temperature. The results indicated that the corrosion resistance of the $\text{Al}_x\text{CrFeMnCu}$ HEAs decreased with increasing Al content. Intergranular corrosion was the primary corrosion type for CrFeMnCu and $\text{Al}_{0.5}\text{CrFeMnCu}$ HEAs, while $\text{Al}_{1.0}\text{CrFeMnCu}$, $\text{Al}_{1.5}\text{CrFeMnCu}$, and $\text{Al}_{2.0}\text{CrFeMnCu}$ HEAs exhibited selective corrosion with enrichment of Al and Cu in the BCC2 phase. The XPS fitting calculations indicated that an increase in the molar ratio of Al led to a decrease in Cr_2O_3 content and an increase in Al_2O_3 content, which weakened the stability and protective properties of the passive film.

1. Introduction

The application of structural alloys in marine environments often involves exposure to high chloride levels, leading to the formation of localized pits or pockmarks on the alloy surface. Although these forms of corrosion result in minimal weight loss, they can progress rapidly and potentially perforate equipment and pipe walls, leading to sudden accidents with significant implications for the economy, environment, and personal safety [1,2]. Related studies have indicated that high-entropy alloys (HEAs) exhibited excellent corrosion resistance, correlating with phase evolution and forming dense passive films composed of a high proportion of oxides and hydroxides [3,4]. The impact of aluminum (Al) incorporation on the corrosion performance of HEAs has been investigated in recent years. Summarizing the available studies, it is evident that the addition of Al facilitates the formation of body-centered cubic (BCC) phases in HEAs. The decline in corrosion resistance correlated with structural inhomogeneity, which manifested via a reduction in the pitting potential as the Al concentration increased [5–7]. Lee et al. [8] studied the corrosion behavior of $\text{Al}_x\text{CrFe}_{1.5}\text{MnNi}_{0.5}$ HEAs in 1 M NaCl solution and observed that the inclusion of Al element resulted in a decreased pitting resistance. Shi et al. [3] investigated the corrosion performance of $\text{Al}_x\text{CoCrFeNi}$ HEAs in chloride solutions and observed that an increase in Al content leads to a decreased in the volume fraction of the chromium (Cr) BCC phase, a decrease in the E_b value, and a decrease in the protective ability of the passivation film. Zhao

et al. [9] also observed similar results in $\text{Al}_x\text{CrFeNi}_{3-x}$ HEAs, where the formation of a porous Al_2O_3 layer reduced the corrosion resistance of the alloy. However, Raza et al. [10] observed that $\text{Al}_x\text{CrFeMoV}$ HEAs exhibited a decreased corrosion current density and an increased breakdown potential with increasing Al content in a 3.5 wt% NaCl solution.

Despite the findings mentioned above, a consensus regarding the effect of Al content on the corrosion performance of HEAs remains elusive. Further exploration of the underlying corrosion mechanisms is needed to establish a clearer understanding. This study developed a series of AlCrFeMnCu HEAs, which exhibited excellent mechanical properties and high-cost effectiveness [11]. In this study, $\text{Al}_x\text{CrFeMnCu}$ HEAs were prepared using the vacuum arc melting technique. The effect of different Al contents on the corrosion behavior of the alloys in a 3.5 wt % NaCl solution was investigated, and the corrosion mechanisms of the alloys in simulated seawater environments were explored. This study provided a reference for the future optimized composition design for the manufacturing of corrosion resistant HEAs and their practical engineering applications.

2. Experimental

2.1. Preparation of alloys

Purity > 99.9 % Al, Cr, iron (Fe), manganese (Mn) and copper (Cu)

* Corresponding author at: School of Material Science and Technology, Lanzhou University of Technology, Lanzhou 730050, China.
E-mail address: fenglis@lut.edu.cn (L. Feng).

metal particles were utilized as raw materials. $\text{Al}_x\text{CrFeMnCu}$ ($x = 0, 0.5, 1.0, 1.5, 2.0$) HEAs were prepared via the vacuum arc melting technique in an argon atmosphere. These alloys were labeled as Al0, Al0.5, Al1.0, Al1.5, and Al2.0, respectively. To ensure a uniform chemical composition, the button ingots underwent at least five remelting circles. All samples were processed using electrical discharge machining (EDM) to achieve dimensions of $10 \times 10 \times 3 \text{ mm}^3$. The electrochemical samples were sealed with epoxy resin, leaving 1 cm^2 of the exposed test area, and the back was welded with Cu wires. The dimensions of the immersed samples and the corrosive medium were consistent with the electrochemical experiments, with an immersion time of 168 h.

2.2. Microstructural characterization

The alloy phase structure was examined using a Cu K α radiation source X-ray diffractometer (XRD, D/MAX2500PC) with tube voltage and current set at 40 kV and 40 mA, respectively. The 2 θ range was acquired at a speed of 5°/min from 20° to 90°. The microstructure and chemical composition of the HEAs were obtained using a field emission scanning electron microscope (FSEM, FEI QUANTA FEG250) enhanced with an energy dispersive spectrometer (EDS, EDAX Elements) and transmission electron microscopy (TEM, FEI TALOS F200S). The chemical composition of the alloy passivation film was analyzed using a monochromatic Al K α radiation source (1486.6 eV) X-ray photoelectron spectrometer (XPS, Thermo Scientific™ K-Alpha™+). The measurements were conducted under a vacuum pressure of less than 10^{-8} mbar and a working power of 100 W. Additionally, the microstructure morphology and elemental distribution after polarization measurements were observed using a laser confocal microscopy (CLSM, LSM800) and an electron probe microanalyzer (EPMA, EPMA-1600), respectively.

2.3. Electrochemical measurements

The $\text{Al}_x\text{CrFeMnCu}$ HEAs were subjected to potentiodynamic polarization (PDP) curve testing in a 3.5 wt% NaCl solution using an electrochemical workstation (CHI760E). The scanning was performed from -1 V vs. Ag/AgCl to $0.5 \text{ V vs. Ag/AgCl}$ at a rate of 0.005 V/s. The working electrode was made of the alloy, the counter electrode was a platinum sheet, Ag/AgCl electrode served as the reference electrode. To minimize the liquid junction potential, a double salt bridge was employed for the reference electrode. Initially, before the test, the open circuit potential (OCP) was measured for 1800 s to attain a stable potential. The parameters for the cyclic polarization curve (CPP) test correlated with the potentiodynamic polarization test. The electrochemical impedance spectroscopy (EIS) test was conducted at the stabilized OCP using a frequency range of $10^5 \text{ Hz}-10^{-1} \text{ Hz}$ and an amplitude of 5 mV. The Mott-Schottky (M-S) test was executed with an amplitude of 10 mV and a frequency of 1000 Hz, spanning from -1 V vs. Ag/AgCl to $0.5 \text{ V vs. Ag/AgCl}$. All tests were repeated three times to ensure data accuracy.

3. Results and discussion

3.1. Microstructure analysis

Fig. 1 shows the XRD patterns of the $\text{Al}_x\text{CrFeMnCu}$ HEAs. The perpendicular bars at the bottom representing the standard diffraction patterns of Fe-Cr BCC solid solution (red lines), Cu monomers (blue lines), and $\text{Cu}_{0.75}\text{Al}_{0.25}$ intermetallic compound (magenta lines). The alloy consisted of face-centered cubic (FCC) and BCC phases. At an Al molar ratio of < 1 , the intensity of the BCC diffraction peaks increased with the addition of Al, while the intensity of the FCC diffraction peak decreased until it became invisible in the Al1.0 alloy. The alloy phase structure changed to BCC as the molar ratio of Al continued to increase. The results indicated that increasing the Al content reduced the FCC phase content and increased the BCC phase content. Additionally, the characteristic peak (110) of the BCC phase exhibited a slight leftward

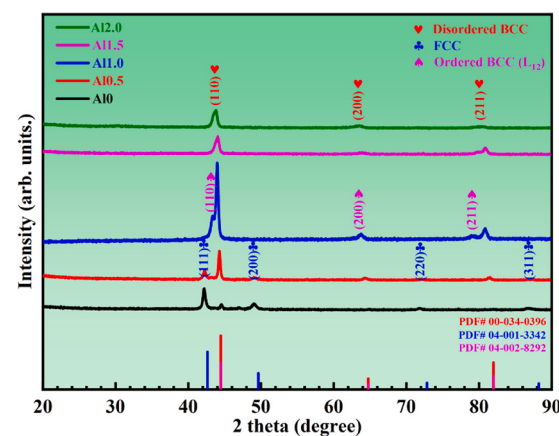


Fig. 1. XRD patterns of the as-cast $\text{Al}_x\text{CrFeMnCu}$ HEAs.

shift, corresponding to the lattice distortion due to the larger atomic radius of the element Al.

Fig. 2 depicts the secondary electron images of the $\text{Al}_x\text{CrFeMnCu}$ HEAs at high and low magnifications, respectively. The five alloys exhibited a microstructure consisting of dark dendrites and bright gray interdendrites. **Table 1** presents the EDS point scan results for the area highlighted in red, indicating that the dendritic (DR) areas were enriched in Fe, Cr, and Mn, while interdendritic (ID) areas were enriched in Al and Cu. The segregation of Cu in the interdendritic region correlates with its more positive enthalpy of mixing (ΔH_{mix}) with other elements. From previous research [11], the dendritic and interdendritic areas of the Al0 and Al0.5 alloys comprised the FCC and BCC phases, while the Al1.0, Al1.5, and Al2.0 alloys consisted of the BCC1 and BCC2 phases, respectively. **Fig. 2(f-j)** depicts the FESEM images of the $\text{Al}_x\text{CrFeMnCu}$ HEAs at high magnification. In the dendritic regions, numerous micrometers to sub-micrometer-sized precipitates were observed. Given an increasing Al molar ratio, the number of particles increased, and their size transformed into an interconnected network structure.

The further identification of crystallographic information and chemical constituents of the precipitated phase was also accomplished by combining TEM-EDS as shown in **Fig. 3**. Based on the selected area electron diffraction (SAED) pattern as shown in **Fig. 3(b)** and (d), it confirms that the matrix in the dendritic region is a disordered Fe-Cr BCC solid solution, and the precipitated phase is an ordered rich Al-Cu BCC structure. The presence of AlCu intermetallic compounds and Fe-Cr solid solution was reconfirmed by high resolution transmission microscopy (HRTEM). In addition, the elemental distribution of the Al1.5 alloy was also given using STEM, and the results are shown in **Fig. 3(g-k)**. It can be seen that Al elements are more uniformly distributed in both phases, Fe, Cr, and Mn elements are enriched in the dendrites, and Cu elements are enriched between the interdendrites. This is consistent with the SEM-EDS results. In addition, the combination of the point scan plots in **Fig. 3(I)** reconfirms that the precipitated phase is an AlCu intermetallic compound. Therefore, based on the TEM analysis results, it can be concluded that the matrix of the $\text{Al}_x\text{CrFeMnCu}$ HEAs in the DR region is a disordered Fe-Cr BCC phase, and ordered rich Al-Cu BCC needle like precipitate in the Fe-Cr BCC regions.

3.2. Corrosion analysis

3.2.1. Immersion experiment

The corrosion performance of $\text{Al}_x\text{CrFeMnCu}$ HEAs in 3.5 wt% NaCl solution was assessed through full immersion experiments. The rate of corrosion (**Table 2**) was determined by calculating the cumulative mass loss. The specific formula is provided in **Eq. (1)**:

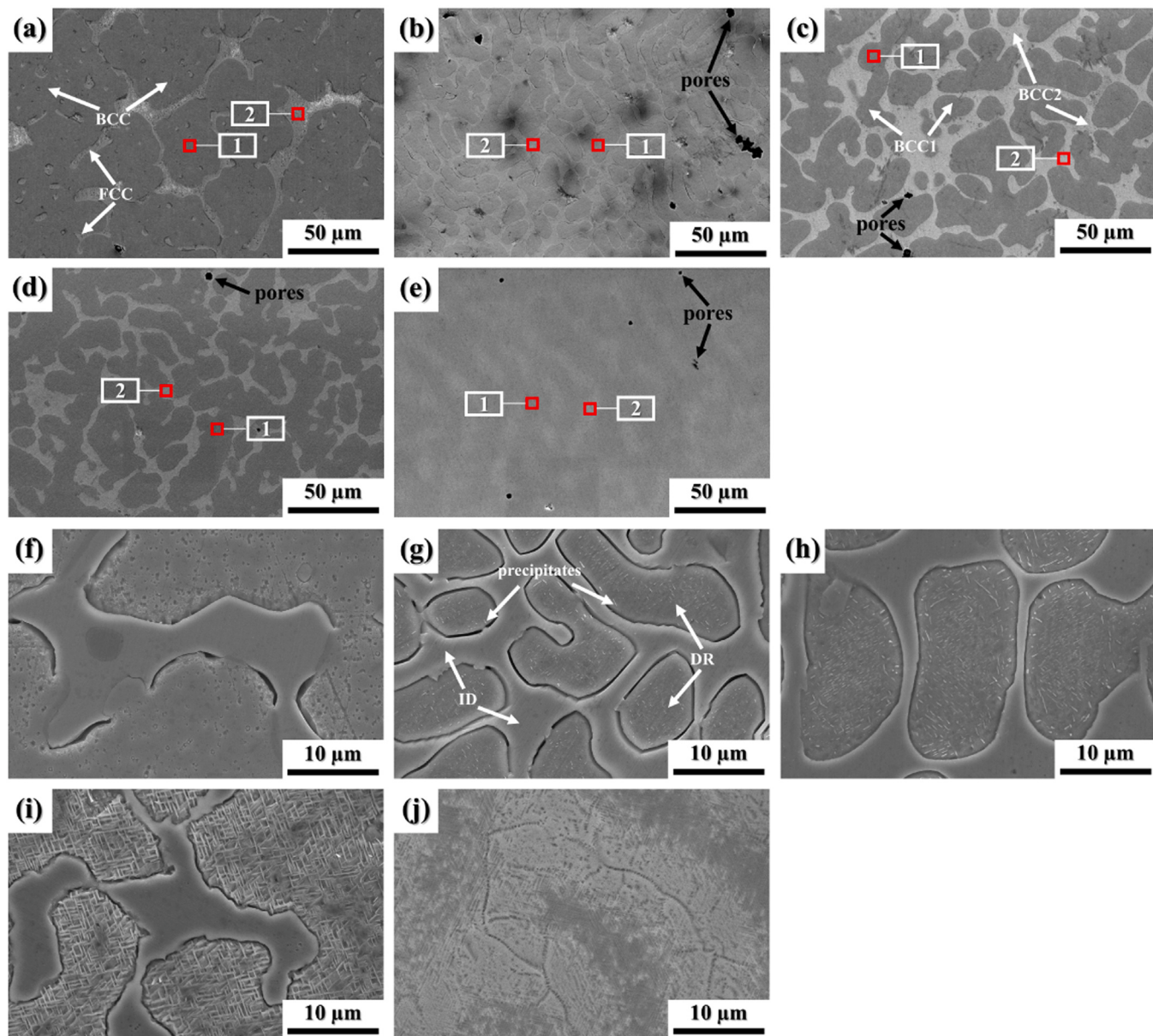


Fig. 2. The low and high magnification microstructures images of the surface of as-cast (a, f) Al0, (b, g) Al0.5, (c, h) Al1.0, (d, i) Al1.5, and (e, j) Al2.0 HEAs.

Table 1
Chemical compositions of different regions in $\text{Al}_x\text{CrFeMnCu}$ HEAs by EDS (at%).

Alloys	Area	Elements (at%)				
		Al	Cr	Fe	Mn	Cu
Al0	1	-	42.38	36.49	19.82	1.31
	2	-	1.56	2.36	32.46	63.62
Al0.5	1	8.79	34.65	32.22	21.76	2.57
	2	10.89	1.31	2.01	22.19	63.59
Al1.0	1	18.35	32.32	28.20	17.27	3.87
	2	22.26	1.21	3.12	15.15	58.25
Al1.5	1	25.70	26.03	22.37	20.00	5.90
	2	29.24	2.95	7.73	15.49	44.59
Al2.0	1	30.95	21.92	18.30	18.67	10.17
	2	34.87	8.44	12.82	16.92	26.95

$$\text{Corrosion rate} = \frac{K \times W}{S \times t \times \rho} \quad (1)$$

In Eq. (1), the constant K has a value of 8.76×10^4 , W represents the mass loss (g), S denotes the exposed area (cm^2), t expresses the immersion time (h) and ρ is the density (g/cm^3). Based on the analysis in Table 2, the corrosion rate of the $\text{Al}_x\text{CrFeMnCu}$ HEAs exhibited an upward trend as the Al content increased.

3.2.2. Potentiodynamic polarization (PDP) tests

The polarization curves for $\text{Al}_x\text{CrFeMnCu}$ HEAs in 3.5 wt% NaCl solution is depicted in Fig. 4. Five alloys exhibited a direct transition from the Tafel region to the stable passive region, bypassing the typical activation-passivation transition region. This behavior indicated spontaneous passivation of the alloys. From these curves, the relevant corrosion parameters can be extracted, as given in Table 3.

From Table 3, it was observed that as the Al content increased, the overall corrosion potential (E_{corr}) decreased, indicating that $\text{Al}_x\text{CrFeMnCu}$ HEAs exhibited increased corrosion tendency. Al0 alloy exhibited the highest pitting potential (E_{pit}) ($-282 \text{ mV}_{\text{Ag}/\text{AgCl}}$), which

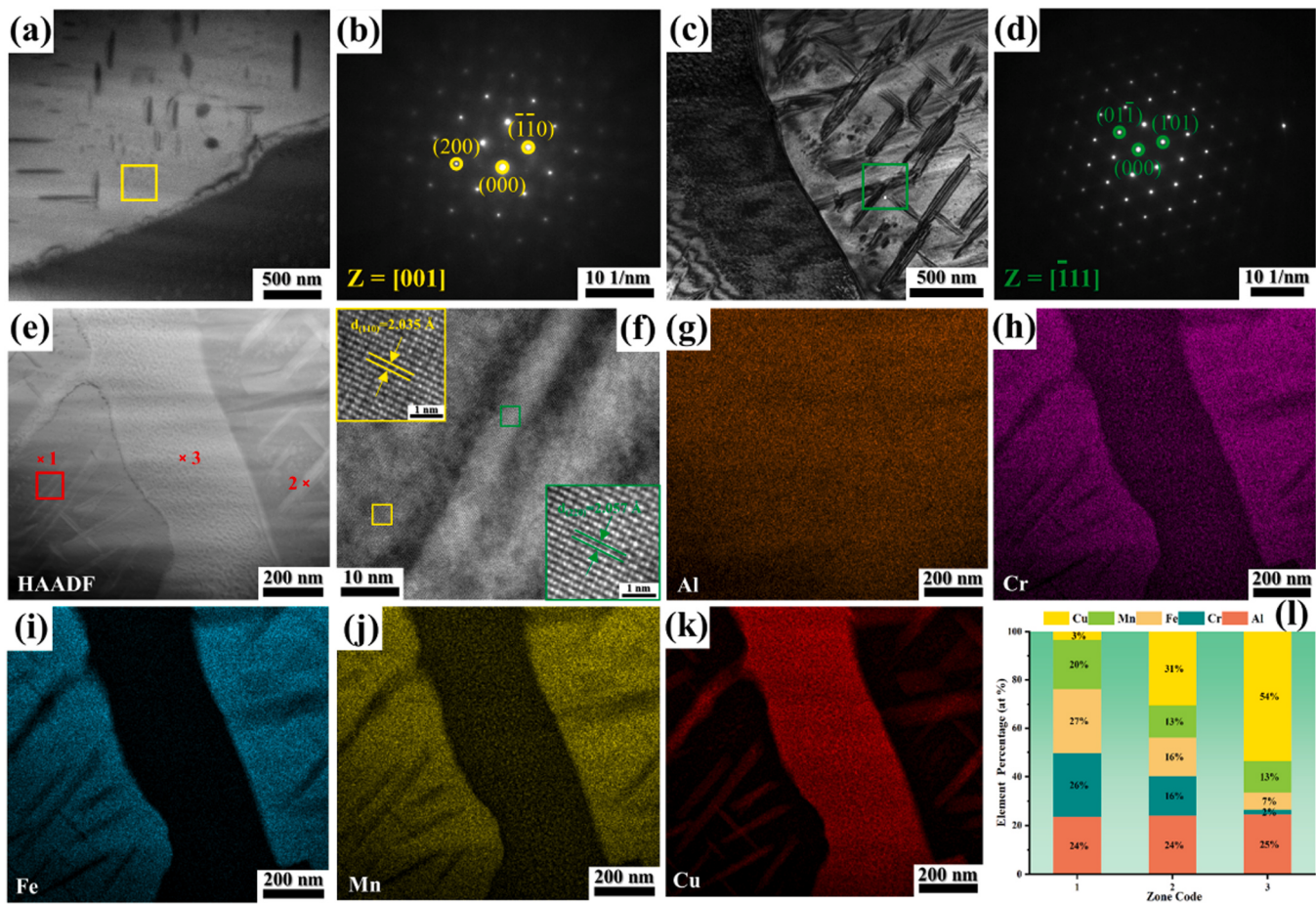


Fig. 3. TEM analysis of Al1.5 HEAs. (a) dark-field (DF) image; (b) corresponding diffraction pattern of the matrix phase labeled with a yellow box in (a); (c) bright-field (BF) image; (d) corresponding diffraction pattern of the precipitated phase labeled with a greener box in (c); (e) High-Angle Annular Dark Field Scanning Transmission Electron Microscope (HAADF) image; (f) High-Resolution transmission electron microscopy (HRTEM) image of the precipitated phase labeled with a red box in (e); (g)-(k) corresponding composition maps of Al, Cr, Fe, Mn, Cu in (e), respectively; (l) corresponding EDS results of 3 points shown in (e).

Table 2
Corrosion rate of the as-cast $\text{Al}_x\text{CrFeMnCu}$ HEAs.

Alloys	Al0	Al0.5	Al1.0	Al1.5	Al2.0
Corrosion rate (mm/y)	0.072	0.080	0.088	0.183	0.220

indicated that it exhibited higher pitting resistance as well as exceptional corrosion resistance. From a thermodynamic perspective, an increased molar ratio of Al results in a higher corrosion tendency for $\text{Al}_x\text{CrFeMnCu}$ HEAs, facilitating the formation of a porous passive film (Al_2O_3) that was ineffective in resisting Cl^- corrosion [12]. Additionally, the increased Al molar ratio resulted in a decreased Cr content, which may also contribute to the reduction in corrosion resistance.

3.2.3. Analysis of microstructure and chemical composition after polarization measurements

In order to further understand the corrosion behavior of $\text{Al}_x\text{CrFeMnCu}$ HEAs, the corrosion morphology after potentiodynamic polarization test is shown in Fig. 5. Corrosion occurs at grain boundaries for Al0 and Al0.5 alloy, as shown in Fig. 5(a-b). Generally, grains and grain boundaries readily constitute corrosion microcells due to the high energy and electrochemical activity of grain boundaries. Cl^- is easy to diffuse through grain boundaries, which are preferentially corroded as anodes. Additionally, the presence of pitting pits near the grain boundaries of the Al0.5 alloy indicated that it exhibited a high corrosion susceptibility. Selective corrosion of Al1.0 and Al2.0 alloys with Al-Cu

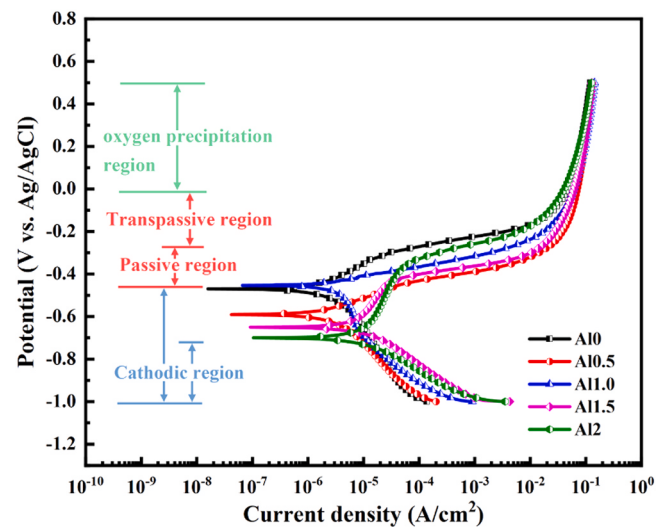


Fig. 4. Linear polarization curves of the $\text{Al}_x\text{CrFeMnCu}$ HEAs in the 3.5 wt% NaCl solution.

rich, and poor Cr phases was observed in Fig. 5(c-d), indicating that the BCC2 phase was more susceptible to Cl^- erosion than the BCC1 phase, could be attributed to the differences in the surface passivation films formed on the two phases. Fig. 5(c) shows residual corrosion products in

Table 3

The corrosion properties of the $\text{Al}_x\text{CrFeMnCu}$ HEAs of polarization tests.

Alloys	E_{corr} (mV vs. Ag/AgCl)	E_{pit} (mV vs. Ag/AgCl)
Al0	-462	-282
Al0.5	-578	-421
Al1.0	-437	-307
Al1.5	-632	-447
Al2.0	-697	-379

the BCC2 phase corrosion region of the Al1 alloy, with the number and size of pitting and corrosion regions further increasing as the Al molar ratio reached 2.0. Selective leaching corrosion was observed at the periphery of the selectively corroded regions, which formed the etch holes or corroded regions as the leaching product was removed (Fig. 5(d)). F, pitting holes were present in the BCC1 phase, which was related to the higher Al content in the BCC1 phase (Table 1) and a weaker passivation film on top.

Fig. 6 depicts the EMPA elemental distribution after polarization measurements of Al0 and Al2 alloys. The low content of Al and Cu oxides in the dashed corrosion region of the BCC2 phase in the Al2 alloy (Fig. 6(b)) indicated the selective dissolution of Al and Cu oxides. This was attributable to the development of a porous Al_2O_3 protective layer (Al-rich) in the BCC2 phase. Additionally, Cu-metal bonding force was weaker compared with other metal-metal bonding [13], leading to the

ease of separation and dissolution of BCC2 phase Cu elements from the alloy matrix. The BCC1 phase, rich in Cr elements, exhibited much milder corrosion compared with the BCC2 phase. Interestingly, the Al2 alloy exhibited severe selective corrosion compared with the slight corrosion of the Al0 alloy. This severe selective corrosion led to the aggregation of Cr elements, forming oxides around the corrosion region. This phenomenon was attributable to the migration of Cr element forming oxides from the BCC1 phase to the vicinity of the BCC2 phase and the re-passivation of the alloy surface. This tendency also indicated that the Cr element forming oxides exhibited a positive promotion effect on the corrosion resistance of the alloy. Furthermore, compared with the Al2 alloy, the Al0 alloy (Fig. 6(a)) exhibited a smaller quantity and size of the corrosion areas, which was attributable to the high presence of Cr oxide. As reported in the literature [3,14], the selective corrosion of the Cr depleted phase in HEAs was due to the formation of a less protective passive film. This resulted from increased Al oxide and decreased Cr oxide content.

Fig. 7 depicts the laser scanning confocal microscopy three dimensional images of Al0, Al1.0, and Al2.0 alloys after polarization measurements. The Al0 alloy (Fig. 7(a)) exhibited preferential corrosion behavior at grain boundaries, while selective corrosion of the BCC2 phase in the Al1.0 and Al2.0 alloys is illustrated in Fig. 7(c-d). Furthermore, the BCC2 phase exhibited a greater depth compared to the BCC1 phase, which correlated with the passive film breakdown and the

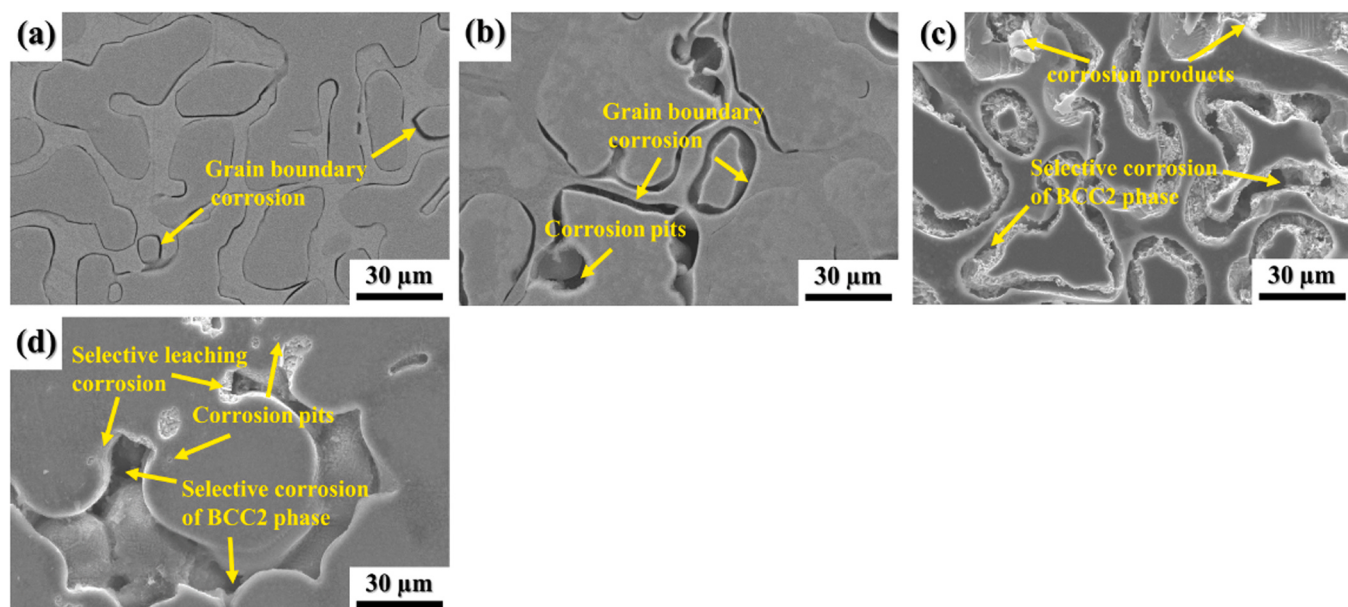


Fig. 5. Surface morphologies of (a) Al0, (b) Al0.5, (c) Al1.0, and (d) Al2.0 HEAs after polarization measurements.

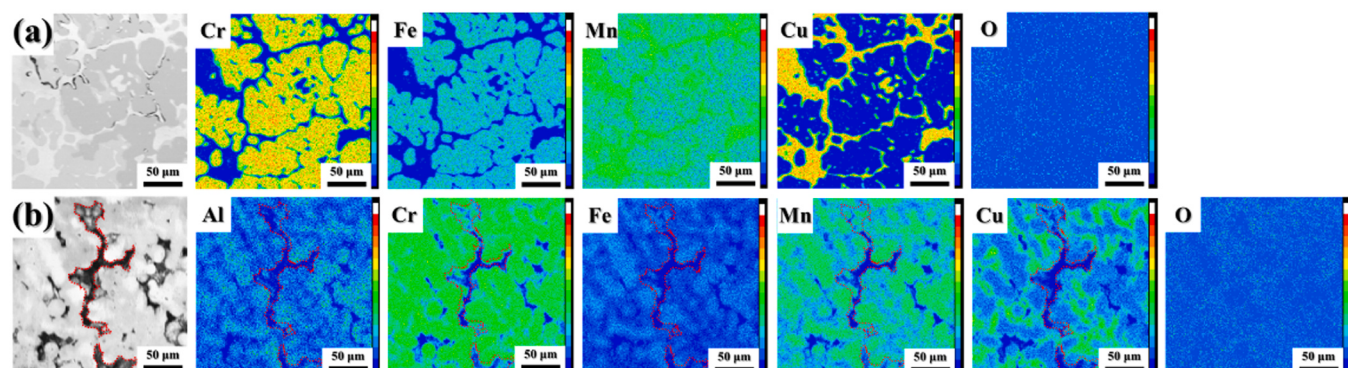


Fig. 6. Electron Probe Microanalysis (EPMA) elemental maps of (a) Al0 and (b) Al2.0 HEAs after polarization measurements.

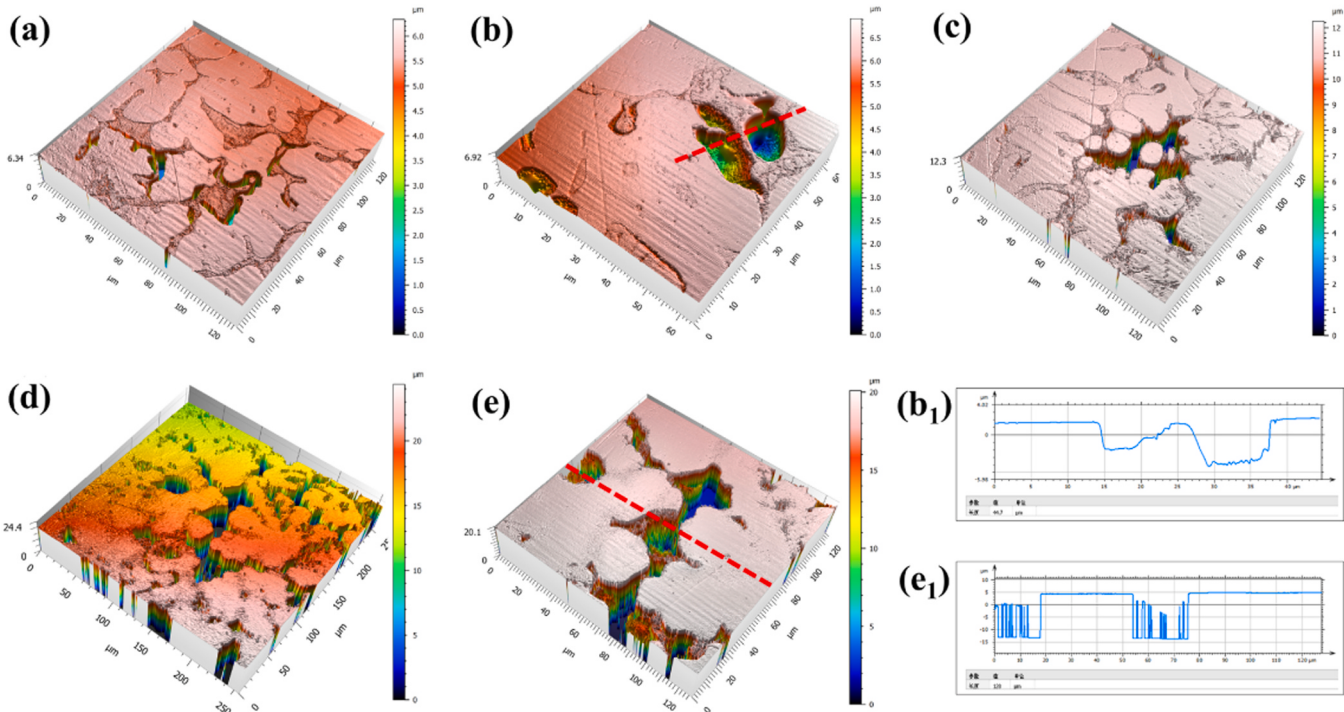


Fig. 7. CLSM Microstructures images of (a-b, b₁) Al0, (c) Al1.0, and (d-e, e₁) Al2.0 alloys after polarization measurements.

preferential dissolution of Al and Cu oxides in the BCC2 phase. Along the marked profiles, the maximum depth of the corrosion pits in the Al0 alloy was $\sim 5 \mu\text{m}$, while in the Al2.0 alloy, the maximum pit depth was $\sim 20 \mu\text{m}$. Additionally, Fig. 7(d) depicts a small number of corrosion pits in the BCC1 phase. As mentioned above, an increased Al content resulted in an increased pit depth and surface corrosion area in the Al_xCrFeMnCu HEAs. Further confirming that the addition of the element Al negatively affects the corrosion resistance of the alloy.

3.2.4. Cyclic potentiodynamic polarization (CPP) tests

The cyclic potentiodynamic polarization (CPP) curves for the five alloys are illustrated in Fig. 8. The protection potential (E_{rp}) is defined as the potential at which the forward scanning curve intersects with the reverse scanning curve. The pitting shift potential (E_{ptp}) denotes the potential at which a transition occurs from anodic current density to cathodic current density. Below the E_{rp} , the sample surface remained free from pitting. Between the E_{rp} and E_b , the existing pits on the sample surface developed and grew continually, however, no new pits were formed. When the applied potential surpassed the E_b , pits on the sample

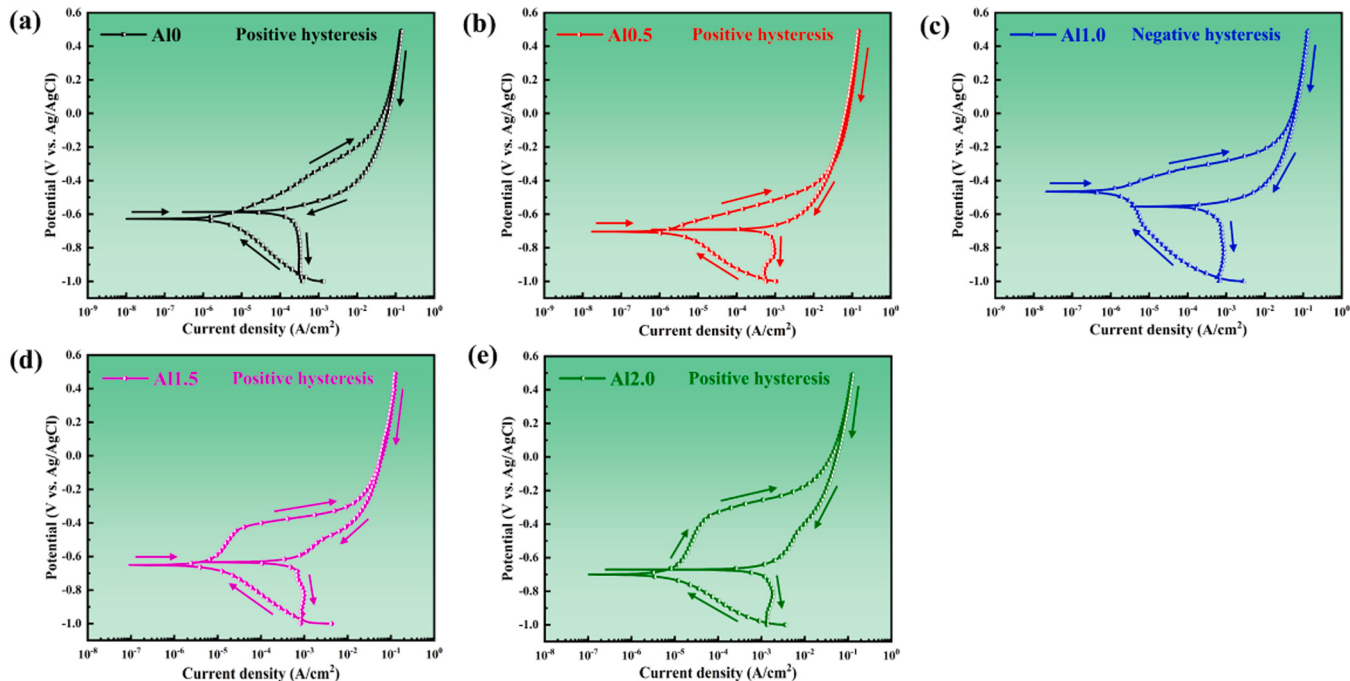


Fig. 8. Cyclic polarization curves of the Al_xCrFeMnCu HEAs immersed in 3.5 wt% NaCl solution.

surface rapidly occurred and developed. Fig. 8(a–b) and (d–e) exhibited the occurrence of a positive hysteresis on the CPP curves of Al0, Al0.5, Al1.5, and Al2. Simultaneously, the E'_b and E_{rp} were higher than the E'_{corr} . Given the report in reference [14,15], this phenomenon indicated that the alloy surface passive film exhibited self-repairing properties. Additionally, for the Al1 alloy, E'_{corr} was greater than E_{rp} , indicating the absence of re-passivation behavior.

Table 4 presents the corrosion parameters obtained by the CPP curves. Based on the analysis, the discrepancy between E'_b and E_{rp} widens with higher Al content. This indicated that the self-repair ability of $\text{Al}_x\text{CrFeMnCu}$ HEAs was reduced by the addition of Al, leading to an increased pitting expansion and a weaker corrosion resistance.

3.2.5. Electrochemical impedance spectroscopy (EIS) tests

Fig. 9(a–b) depict the Nyquist and Bode diagrams for all five alloys at OCP. The Nyquist plots of all alloys exhibited semicircle-like characteristics with the centers depressed towards the X-axis, indicating that the formation mechanism of the corrosion product film was not affected by the variation in Al content. The diameters of the capacitive semicircles decreased in the following trend: $\text{CrFeMnCu} > \text{Al}_{0.5}\text{CrFeMnCu} > \text{Al}_{1.0}\text{CrFeMnCu} > \text{Al}_{1.5}\text{CrFeMnCu} > \text{Al}_{2.0}\text{CrFeMnCu}$. This indicated that as the Al content increased, the charge transfer resistance of $\text{Al}_x\text{CrFeMnCu}$ HEAs progressively reduced, resulting in a decreased corrosion resistance. Furthermore, according to the corresponding Bode plot (Fig. 9(b)), the impedance module reduced as the frequency increased within the low-frequency range. Al0 and Al2 alloys reached the maximum level ($\sim 6.5 \times 10^3 \Omega\cdot\text{cm}^2$) and minimum level ($\sim 1.1 \times 10^3 \Omega\cdot\text{cm}^2$) impedance modulus, respectively. When the frequency ranged from 10^1 Hz to 10^2 Hz and the phase angle reached its maximum ($\sim 80^\circ$), it indicated that non-uniform surfaces led to non-ideal pure capacitive behavior, corresponding to the homogeneity of the material surface [16]. Additionally, the impedance modulus tended to a broad plateau in the range of 10^2 Hz - 10^5 Hz, indicating the pseudo-capacitive nature of the corrosion product, and introducing constant phase angle elements (CPE) to replace the ideal purely capacitive. The following equation (Eq. (2)) was used to calculate the impedance of the CPE (Z_{CPE}). Based on the above analysis, the simulation was equivalent to an electron circuit (EEC) modeled as a circuit consisting of two-time constants (Fig. 10), and Table 5 presents the associated fitting values.

$$Z_{CPE} = \frac{1}{Q(\omega i)^n} \quad (2)$$

In Eq. (2), Q represents the admittance of CPE, ω denotes the angular frequency, i symbolizes the imaginary unit ($i^2 = -1$), and n denotes the exponent for quantifying surface non-uniformity ($0 \leq n \leq 1$). Based on the fitting equivalent circuit model ($R_s(Q_1(R_f(Q_2R_{ct})))$), all five alloys exhibited low χ^2 values, indicating an exceptional fit quality of the circuit model used. R_s symbolizes electrolyte resistance, R_f denotes passive film resistance, R_{ct} symbolizes charge transfer resistance between passive film and substrate, CPE₁ symbolizes capacitance of the passive film, and CPE₂ signifies double layer capacitance. Table 5 presents the values of n_1 and n_2 for the Al0, Al0.5, and Al1.0 alloys, which were ~ 1 , indicating that their passive films exhibited capacitance properties similar to smooth surfaces [17]. The fitted R_{ct} for $\text{Al}_x\text{CrFeMnCu}$ HEAs was significantly higher than R_f . Therefore, it is reasonable to assume

Table 4

Corrosion parameters of the $\text{Al}_x\text{CrFeMnCu}$ HEAs of cyclic polarization measurements in 3.5 wt% NaCl solution.

Alloys	E'_{corr} (mV vs. Ag/AgCl)	E'_b (mV vs. Ag/AgCl)	E_{rp} (mV vs. Ag/AgCl)	$E'_b - E_{rp}$ (mV)	E_{ptp} (mV vs. Ag/AgCl)
Al0	-628	-476	-585	109	-587
Al0.5	-704	-532	-690	158	-692
Al1.0	-465	-369	-554	185	-553
Al1.5	-650	-439	-634	195	-633
Al2.0	-700	-360	-671	331	-669

that the strong dependence of the charge transfer resistance on the passive film represents the corrosion resistance of the material. The Al0 alloy exhibited the largest R_{ct} ($6975 \Omega\cdot\text{cm}^2$) in the series of alloys investigated in this study, indicating that it exhibited the slowest corrosion rate in the electrolyte solution, forming a more stable passivation film and a stronger resistance to Cl^- erosion. Thus, with decreasing Al content, the R_{ct} value of the $\text{Al}_x\text{CrFeMnCu}$ HEAs increased, indicating that the charge transfer of the alloy process became more challenging. The polarization resistance ($R_p = R_f + R_{ct}$) strongly depending on the passive film can be adopted to evaluate the corrosion resistance of materials [18]. It was found that R_p decreased from Al0 alloy ($6.98 \times 10^6 \Omega\cdot\text{cm}^2$) to Al1.5 alloy ($2.9 \times 10^3 \Omega\cdot\text{cm}^2$), and Al2.0 alloy had the lowest ($2.2 \times 10^3 \Omega\cdot\text{cm}^2$), revealing the decrease of corrosion resistance. Furthermore, the CPE₁ and CPE₂ values increased with an increased Al molar ratio, while R_f exhibited the opposite trend, indicating a decrease in the stability and densification of the passive film. This was attributable to a less effective Al_2O_3 layer being formed due to a higher Al content. Thus, the relative fitting parameters further confirmed the polarization and EIS results.

The thickness of the passive film (d) was determined from the fitted EIS values, as delineated in Eq. (3) [15,19]:

$$d = \frac{(\varepsilon\varepsilon_0 S)}{C} \quad (3)$$

Where ε_0 and ε represent the vacuum dielectric constant ($8.8542 \times 10^{-14} \text{ F cm}^{-1}$) and the relative dielectric constant of the passivation film, respectively, and S stands for the geometric area. In this study, 2 times the geometric area was used for calculation [20,21]. Based on experience [22–24], a dielectric constant value of 12 was usually assigned to the passive film in HEAs. C is the capacitance of the passive film of the alloys. The effective capacitance was obtained from the Brug's formula, and the calculation is as follows [25]:

$$C = (CPE_{dl})^{\frac{l}{n}} \left(\frac{I}{R_s} + \frac{I}{R_{ct}} \right)^{\frac{n-l}{n}} \quad (4)$$

In Eq. (4), CPE_{dl} represents the CPE₂ in the equivalent electron circuit model, n denotes the CPE exponent, and R_s and R_{ct} are shown in Table 5. Based on Eq. (4), the capacitance of passive film (C_1) and electric double layer (C_2) were derived from CPE₁ and CPE₂, which were listed in Table 5, respectively. Thus, the thickness of the passive film gradually decreased as the molar ratio of Al increased as follows: Al0 (2.54 nm) > Al0.5 (2.52 nm) > Al1.0 (1.36 nm) > Al1.5 (0.98 nm) > Al2.0 (0.72 nm). Where the thickness of the passivation film of the Al0 alloy (2.54 nm) was more than three times of the Al2.0 alloy (0.72 nm), which was consistent with the change in corrosion resistance. Besides, the calculated passive film thicknesses in the nanometer level were similar to that of some HEAs in 3.5 wt% NaCl solution at OCP condition based on the EIS data [26,27].

3.3. Passivation film characteristics

3.3.1. XPS analysis

As indicated by the PDP curves and the EPMA mapping, a protective passivation film formed on the surface of the $\text{Al}_x\text{CrFeMnCu}$ HEAs in the 3.5 wt% NaCl solution. The properties of the film depend on their chemical composition, which directly affects the corrosion resistance of the alloy. In order to obtain more information about the passivation film, XPS was used to analyze the chemical composition of the film.

The high-resolution spectra of the passivation films of the $\text{Al}_x\text{CrFeMnCu}$ HEAs were obtained using Gauss - Lorentz fitting, as displayed in Fig. 11. The $\text{Al}^{2p_{3/2}}$ spectrum is divided into two peaks, representing Al^0 (72.5 eV) and Al_2O_3 (74.5 eV), with Al_2O_3 being the primary component. The dashed line represents the Cu^{3p} orbital peak. The $\text{Cr}^{2p_{3/2}}$ spectrum at 573.9 eV, 576.3 eV, 577.7 eV, and 579.1 eV was fitted to Cr^0 , Cr_2O_3 , Cr(OH)_3 , and CrO_3 . From the $\text{Mn}^{2p_{3/2}}$ spectrum,

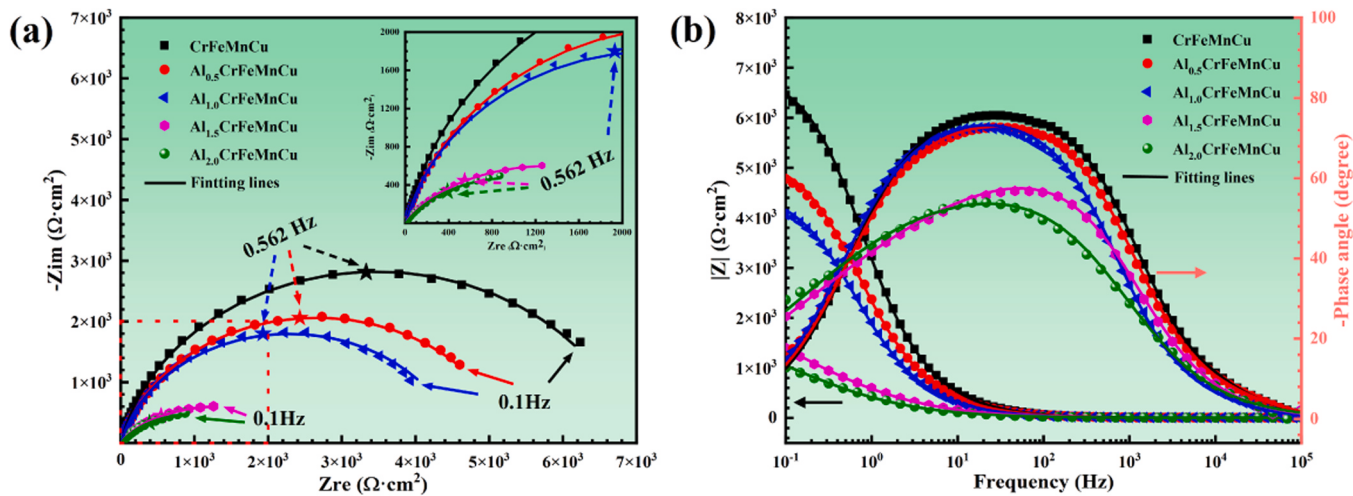


Fig. 9. (a) Nyquist plots and (b) Bode plots of the $\text{Al}_x\text{CrFeMnCu}$ HEAs in 3.5 wt% NaCl solution.

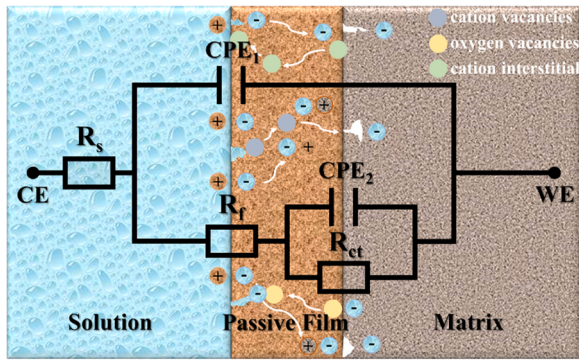


Fig. 10. EEC and PDM models for interpretation of the EIS data of the $\text{Al}_x\text{CrFeMnCu}$ HEAs in 3.5 wt% NaCl solution.

four peaks were observed, including Mn^0 (638.4 eV), Mn_2O_3 (640.2 eV), MnO_4 (641.8 eV), and $\text{Mn}_{\text{ox}}^{2+}\text{sat}$ (647.2 eV). The $\text{Fe}2\text{p}_{3/2}$ spectrum was divided into five peaks, representing 706.5 eV for Fe^0 , 709.2 eV for FeO , 710.8 eV for Fe_2O_3 , 712.8 eV for FeOOH , and 716.2 eV for $\text{Fe}_{\text{ox}}^{2+}\text{sat}$. Notably, to differentiate between Cu^0 and $\text{Cu}_{\text{ox}}^{1+}$ peaks in the $\text{Cu}2\text{p}$ orbital was difficult due to their overlap. Therefore, they were represented as $\text{Cu}^0 + \text{Cu}_{\text{ox}}^{1+}$. A further distinction can be made by scanning the Cu Auger spectrum (Cu LMM) to differentiate $\text{Cu}_{\text{ox}}^{1+}$ from $\text{Cu} + \text{Cu}_{\text{ox}}^{2+}$. Three peaks located at O^{2-} (530.3 eV), OH^- (531.6 eV), and adsorbed water (533 eV) made up the O1s spectrum. O^{2-} and OH^- were associated with the aforementioned metal oxides and hydroxides [28].

To further analyze the differences in elements and valence states within the passive film of $\text{Al}_x\text{CrFeMnCu}$ HEAs, the atomic content (C_M) of individual metal elements within the passive film is given by Eq. (5) [29,30]:

$$C_M = \frac{I_M/S_M}{\sum I_i/S_i} \quad (5)$$

Table 5
EEC parameters for interpretation of the EIS data of the $\text{Al}_x\text{CrFeMnCu}$ HEAs.

Alloys	R_s ($\Omega \cdot \text{cm}^2$)	CPE_1 ($10^{-5}\Omega^{-1}\text{cm}^{-2}\text{s}^n$)	n_1	R_f ($\Omega \cdot \text{cm}^2$)	CPE_2 ($10^{-5}\Omega^{-1}\text{cm}^{-2}\text{s}^n$)	n_2	R_{ct} ($\Omega \cdot \text{cm}^2$)	$C_1 (10^{-6} \text{ F. cm}^2)$	$C_2 (10^{-6} \text{ F. cm}^2)$	$\chi^2 (10^{-3})$	d (nm)
Al0	6.35	1.02	0.98	3.05	4.14	0.83	6975	8.38	7.65	0.27	2.54
Al0.5	6.27	1.25	0.96	2.23	6.13	0.81	5336	8.43	9.69	0.38	2.52
Al1.0	7.30	2.25	0.96	2.22	7.12	0.80	4602	15.65	10.75	0.53	1.36
Al1.5	5.66	9.99	0.83	1.35	46.68	0.46	2849	21.59	0.44	0.46	0.98
Al2.0	5.77	28.09	0.74	0.84	49.89	0.43	2165	29.36	0.20	0.93	0.72

Where the I_M represents the peak intensity corresponding to the area of each element, while S_M denotes the sensitivity factor for that element. Fig. 12 depicts the semi-quantitative fitting calculations of the overall elemental composition of the passivation films of the five alloys, the atomic ratio components of the metallic and oxidation states of each element, and the results of the overall XPS fitting. Fig. 12(a) shows the highest Cr content in the Al0 alloy passivate film. As the Al molar ratio increased, the Al element replaced the Cr element to become the primary constituent within the passivation film, while the contents of the Cr, Mn, Fe, and Cu decreased. This was attributable to the increased Al molar ratio in the alloy, which resulted in a relative decrease in the content of other elements. Furthermore, based on Fig. 12(b), the content of $\text{Cu}_{\text{ox}}^{2+}$ was relatively constant with an increasing molar ratio of Al, while the contents of Cr, Fe, Mn oxides, and hydroxides decreased. Among them, the reduction in the Cr oxides was the most severe. Additionally, in the passivation films of Al0, Al0.5, Al1.0, and Al1.5 alloys, the Cr_2O_3 content was higher than that of the other three oxides or hydroxides, and its variation was particularly evident as the molar ratio of the Al decreased from 1.5 to 0 (Fig. 12(c)). It has been reported that dense Cr_2O_3 contributed to the stability and homogeneity of the passive film, CrO_3 was detrimental to film stability, and Al oxides tended to form porous thin film structures [31,32]. The lower Cr_2O_3 content and higher Al_2O_3 content of the $\text{Al}_x\text{CrFeMnCu}$ alloys elucidated the decreased corrosion resistance as the Al molar ratio increased. Especially for the Al2 alloy, the CrO_3 content was greater than Cr_2O_3 and the non-dense Al_2O_3 was the primary component of its passivates film, leading to its weaker corrosion resistance among the five alloys. Moreover, combining Fig. 12 (b–c), it was found that compared with the Al2 alloy, the other alloys exhibited more unoxidized metals. According to the results of [33], the corrosion resistance of the alloys was enhanced by a mixture of metal oxides and unoxidized metals. Unoxidized metals played a crucial role in impeding the transmission of point defects, adjusting strain, and promoting the formation of barrier layers at the metal/film and film/solution interfaces. This, in turn, resisted the adsorption of depolarizing

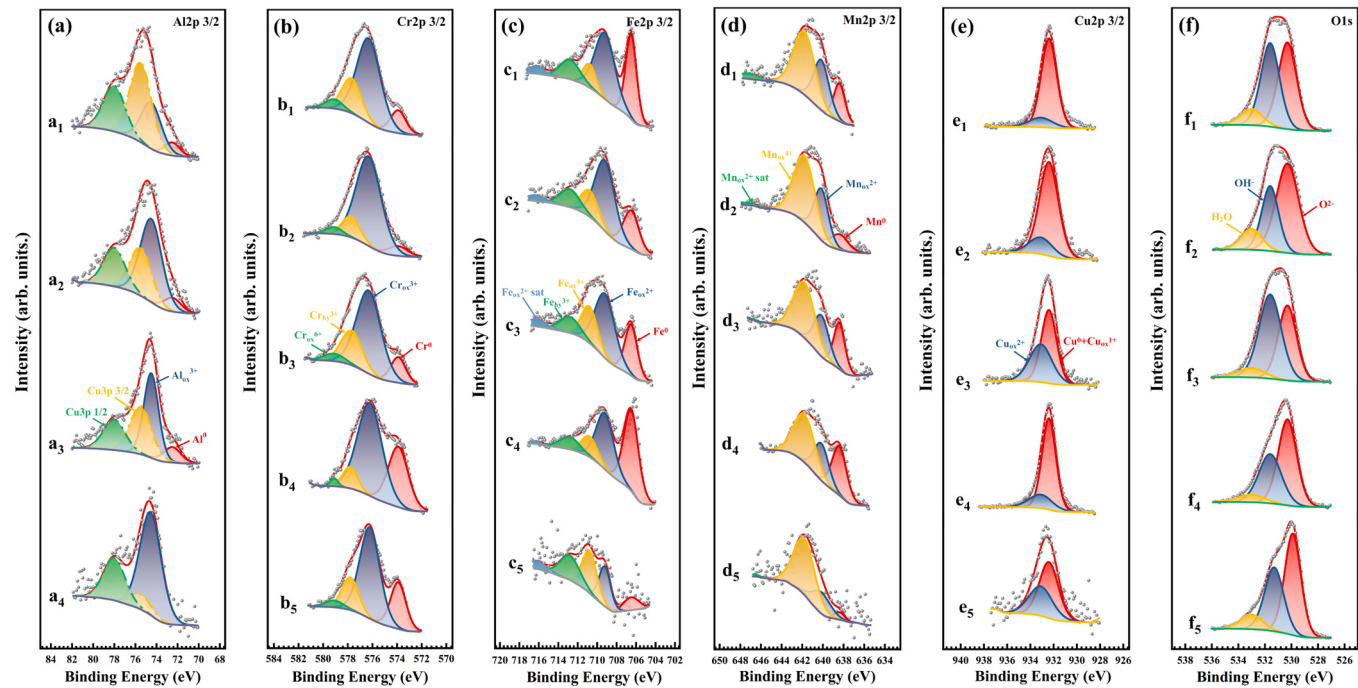


Fig. 11. XPS analysis was performed on the $\text{Al}_x\text{CrFeMnCu}$ HEAs after the PDP measurements. (a-f) the high-resolution XPS spectra assigned to Al 2p_{3/2}, Cr 2p_{3/2}, Fe 2p_{3/2}, Mn 2p_{3/2}, Cu 2p_{3/2}, and O 1 s, respectively.

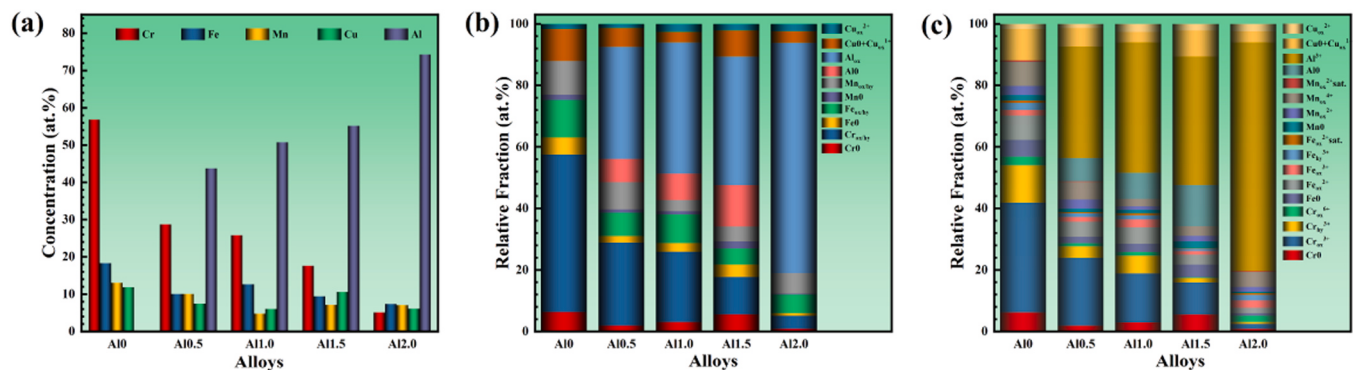


Fig. 12. (a) The overall composition of the passive film. (b) Relative fraction of oxidized and metallic states for $\text{Al}_x\text{CrFeMnCu}$ HEAs elements in the passive film. (c) The fitting valences state of all elements from XPS results.

agents (H^+ , M^{n+} , Cl^-) and enhanced the protective properties of the passivation film. The passivation film of Al2 alloy also exhibited a low content of unoxidized metal, contributing to its diminished corrosion resistance. Finally, the high content of Al elements, especially Al_2O_3 , and the low content of Cr oxides weakened the stability and protective properties of the passive film.

3.3.2. Mott-Schottky analysis

Additionally, the analysis of the chemical composition, and Mott-Schottky (M-S) tests [34,35] were conducted to examine the semiconductor properties and carrier density of the passivated films. According to the M-S mature theoretical model [36,37], the space charge capacitance (C) was determined using the Eq. (6) and Eq. (7):

$$\frac{I}{C^2} = \frac{2}{\varepsilon \varepsilon_0 e N_D} (E - E_{FB} - \frac{kT}{e}) \quad \text{for } n-\text{type semiconductor} \quad (6)$$

$$\frac{I}{C^2} = -\frac{2}{\varepsilon \varepsilon_0 e N_A} (E - E_{FB} - \frac{kT}{e}) \quad \text{for } p-\text{type semiconductor} \quad (7)$$

Where ε and ε_0 refer to Section 3.2.5, e represents the electronic charge (1.602×10^{-19} C), while N_D and N_A denote the donor and acceptor densities of the n-type and p-type semiconductors, respectively. Additionally, E denotes the applied voltage, E_{FB} represents the flat band potential, the Boltzmann constant (1.38×10^{-23} J K⁻¹) is expressed as k , and T signifies the absolute temperature.

The M-S curves of Al0, Al0.5, Al1.0, and Al2.0 alloys are depicted in Fig. 13(a). Three linear regions were observed. The passivation film exhibited p-type semiconductor behavior within the negative slope region I (from -0.93 V vs. Ag/AgCl to -0.67 V vs. Ag/AgCl), indicating the prevalence of cation vacancies as primary acceptors, such as FeO , CuO , and Cr_2O_3 . The passivation film exhibited n-type semiconductor behavior within the positive slope region II (from -0.67 V vs. Ag/AgCl to -0.20 V vs. Ag/AgCl), indicating the prevalence of oxygen vacancies or cationic interstitials, such as Al_2O_3 , Fe_2O_3 , and FeOOH , as the primary donors. Based on the XPS elemental valence state content (Fig. 12(c)) and the M-S results, the primary anodic polarization processes were summarized as follows:



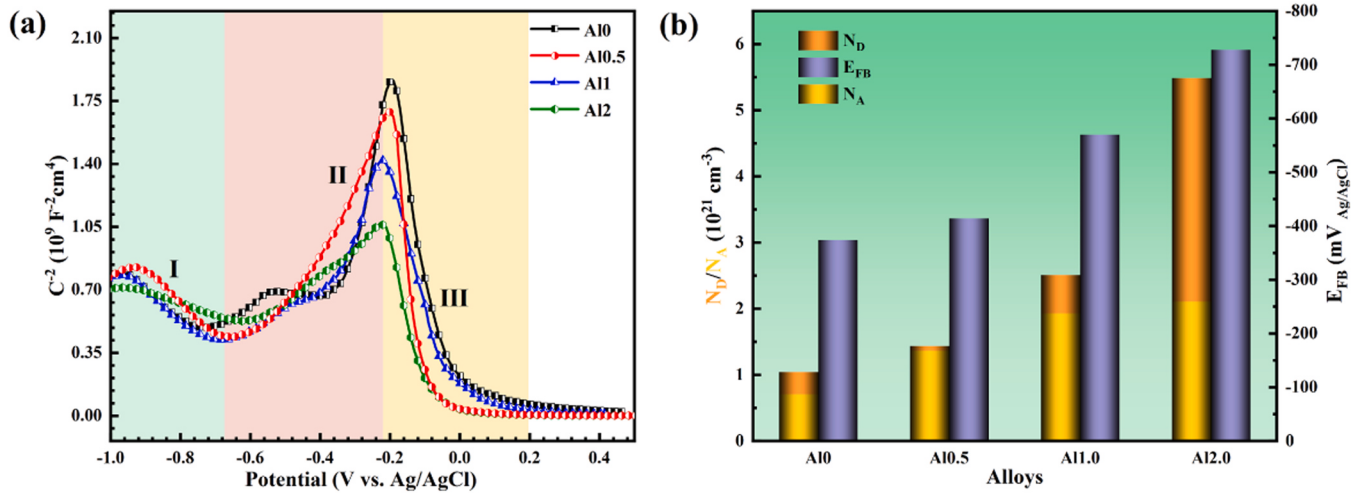
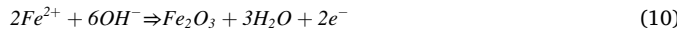
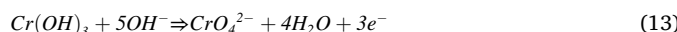
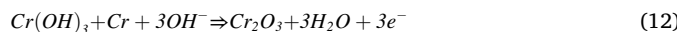


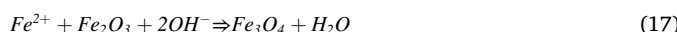
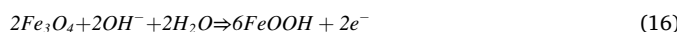
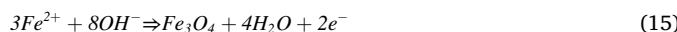
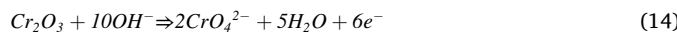
Fig. 13. (a) Mott-Schottky plots of the passive film. (b) N_D , N_A , and E_{FB} values of the passive film.



In this study, the order of the reaction formulae was independent of the order of oxide formation on the surface of the alloy, which corresponded to the magnitude of the Gibbs free energy (ΔG_f°) of the oxides formed by the elements in the alloy. As the applied voltage continues to increase, as depicted in region III (from -0.20 V vs. Ag/AgCl to 0.19 V vs. Ag/AgCl), the passivation film exhibited p-type semiconductor characteristics. The main possible reactions that occurred were summarized as follows:



Or:



Reactions (13), (14), (17), and (18) indicated that the passive film ranged from -0.2 V vs. Ag/AgCl to 0.19 V vs. Ag/AgCl, undergoing dissolution of low-valent metal ions and oxygen precipitation reactions, which led to the destabilization of the passive film. The rise in current density when the potential in Fig. 4 exceeded -0.2 V also confirmed the occurrence of these reactions. From the M-S curve, the data points with a good linear relationship were selected for fitting. The calculations for N_D and N_A were performed using Eq. (6) and Eq. (7), and the results are depicted in Fig. 13(b). With increasing Al content, the values of N_D and N_A exhibited an increasing trend, specifically: CrFeMnCu ($1.04 \times 10^{21} \text{ cm}^{-3}$, $7.09 \times 10^{20} \text{ cm}^{-3}$) $<$ Al_{0.5}CrFeMnCu ($1.44 \times 10^{21} \text{ cm}^{-3}$, $1.56 \times 10^{21} \text{ cm}^{-3}$) $<$ Al_{1.0}CrFeMnCu ($2.51 \times 10^{21} \text{ cm}^{-3}$, $1.93 \times 10^{21} \text{ cm}^{-3}$) $<$ Al_{2.0}CrFeMnCu ($5.49 \times 10^{21} \text{ cm}^{-3}$, $2.11 \times 10^{21} \text{ cm}^{-3}$). This indicated that the charge carrier density of the alloy increased with the amount of the Al present. The electrochemical response between the Al_xCrFeMnCu alloy and the solution increased with increasing oxide and hydroxide

defects in the inner and outer layers. Furthermore, the point defect model (PDM) posited that oxygen vacancies or cationic interstitials were created at the interface between the metal substrate and film, which was subsequently utilized at the interface between the film and solution, while cation vacancies exhibited a contrasting behavior, this is illustrated in Fig. 10 of the EEC model. In this study, a significant amount of n-type point defects in the Al_xCrFeMnCu alloy, according to the research findings in references [38–40], facilitated the migration of metal ions during the corrosion process. Meanwhile, oxygen vacancies and cation interstitial atoms accelerated the transfer of electrons at the interface between the film and the electrolyte, adsorbing more Cl⁻, and promoting the nucleation and growth of pits. The minimum N_D value for the Al0 alloy reached $1.04 \times 10^{21} \text{ cm}^{-3}$, indicating that its surface formed a passive film with denser and fewer defects and exhibited excellent resistance to pitting corrosion, which is also reflected in the fact that its pitting potential exceeds that of other alloys. The N_D value increased with higher Al content, indicating the enhanced sensitivity to pitting nucleation and the adsorption binding energy of the Cl⁻, and the corrosion resistance of the alloy tended to deteriorate.

3.4. Corrosion mechanism of the Al_xCrFeMnCu HEAs

Because of the previous discussion, Fig. 14 illustrates the corrosion mechanism of the Al_xCrFeMnCu HEAs in 3.5 wt% NaCl solution. For the Al0 and Al0.5 alloys with the organization of FCC+BCC phases, chloride ions initially aggregated on the oxides and hydroxides formed on the surface of the alloy. The passive film was disrupted by chloride ion adsorption due to weak grain boundary stability, resulting in the exposure of the substrate to the Cl⁻ solution, and forming multiple small pits (Fig. 14(a₁)). As the corrosion process progressed, both the passivation film intact and locally damaged areas constituted a large cathode-small anode, accelerating the formation and development of pitting nuclei, which in most cases grew further and formed etch holes. Fig. 14(a₂–a₃) depict the acidic self-catalytic process of pit development at the alloy grain boundaries. Initially, anodic dissolution of the metal occurred within the pits at the grain boundaries as follows:



Meanwhile, the electrons released from the anodic reaction migrated to the outer surface of the pit mouth, hindering corrosion around the pitting hole (Fig. 14(a₂)). The reduction of oxygen at the cathode occurred on the outer surface adjacent to the orifice, which is expressed as follows:



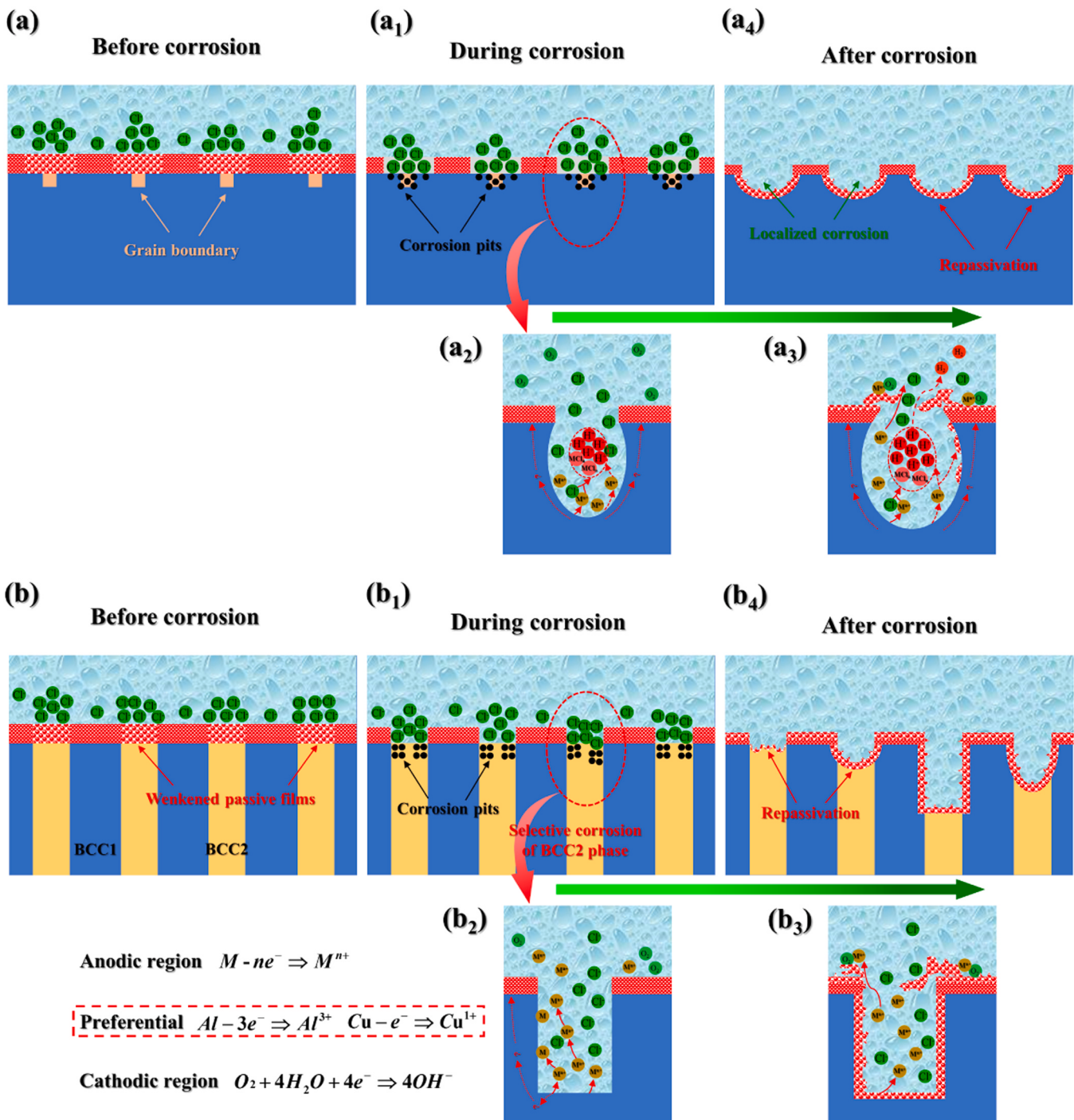


Fig. 14. Schematic illustration depicting the corrosion mechanisms of the as-cast of (a-a₄) Al0, Al0.5, and (b-b₄) Al1.0, Al1.5, and Al2.0 HEA specimens in 3.5 wt% NaCl solution.

Additionally, owing to the PH rise at the orifice, anode dissolved metal ions, as part of the outward migration of the secondary reaction, formed corrosion products piled up in the orifice, restricting the hole inside and outside the material transmission, and promoting the degree of cationization of the metal in the hole. A large number of Cl⁻ migrated to the hole to form metal salts, and hydrolysis occurred as follows:



This led to local acidification in the hole to form an activated-passivated corrosion cell. Thus, the pitting corrosion developed in the form of autocatalysis (Fig. 14(a₃)). However, the development of pitting

did not continue due to the excellent self-repairing ability of the Al0 and Al0.5 alloy passivation film (Fig. 14(a₄)).

The corrosion mechanism of Al1.0, Al1.5, and Al2.0 alloys is shown in Fig. 14(b-b₄). During the early stages of corrosion, Cl⁻ was adsorbed in the uneven aggregation on the alloy surface, and as the chloride complex ions replaced the surface oxides and hydroxides on the BCC2 phase of the alloy, the passivation film was destroyed and a substantial pitting crater was formed. Thus, the growth and development mechanism of the crater is as discussed above. Fig. 14(b₂-b₄) depict the process of selective dissolution of the BCC2 phase. Initially, the multicomponent elements (M = Al, Cu) preferentially ionized and dissolved in the reaction (Eq.

(19). Part of the ionized metal ions dissolved into the solution through convection and disturbed diffusion, while another part participated in the cathodic reaction to form corrosion products that covered the periphery of the holes (Fig. 14(b₃)). Meanwhile, as shown in the reaction, it promoted the depolarization of oxygen (Eq. (20)). Deteriorated metastable pits surfaces attached to plenty of Cl⁻ ions also gave rise to preferential corrosion on BCC2 phase enriched in Al and Cu with the development of corrosion process. The metastable corrosion pits grew and developed into corrosion areas. Due to the self-repair ability of the passive film, the corrosion areas did not continue to expand indefinitely (Fig. 14(b₄)). Furthermore, the difference in composition of the two phases caused the reduction in the protection of passive films, which got worse as the Al molar ratio increased (Fig. 5). Thus, corrosion resistance of Al_xCrFeMnCu HEAs system in 3.5 wt% NaCl solution decreased with the increase of Al content.

4. Conclusions

This study investigated the impact of varying Al content on the corrosion behavior and mechanism of Al_xCrFeMnCu HEAs in a 3.5 wt% NaCl solution. The main findings are summarized below:

- (1) The Al0 and Al0.5 alloys exhibited a combination of FCC and BCC phases. With increasing Al content, the Al1.0, Al1.5, and Al2.0 alloys transformed into BCC1 and BCC2 phases. Notably, in the dendrite region, fine needle-like ordered Al-Cu rich BCC precipitates were observed from disordered Fe-Cr BCC matrix phase.
- (2) The corrosion resistance of Al_xCrFeMnCu HEAs decreased with increasing Al content, evident through the reduction of E_{corr}. This was accompanied by a decreased R_{ct} value and passivation film thickness, as well as an increase in N_D and N_A values.
- (3) Grain boundary corrosion was the primary type of corrosion for Al0 and Al0.5 alloys, while the corrosion types of Al1.0, Al1.5, and Al2.0 alloys were primarily selective corrosion of the BCC2 phase. In addition, XPS analysis shows that the increase of Al molar ratio mainly leads to the decrease of Cr₂O₃ content and the increase of Al₂O₃, which weakens the stability and protection of passivation film.

CRediT authorship contribution statement

Li Feng: Writing – review & editing, Conceptualization. **Yang Yang:** Writing – original draft, Methodology, Investigation, Data curation, Conceptualization. **Yanchun Zhao:** Writing – review & editing, Conceptualization. **Kai Ma:** Writing – review & editing. **Junpeng Cui:** Writing – review & editing.

Declaration of Competing Interest

The authors declare that they have no known competing financial interests or personal relationships that could have appeared to influence the work reported in this paper.

Data Availability

Data will be made available on request.

Acknowledgements

The authors gratefully appreciate the financial supports from the Project of CNNC Nuclear Power Operation Management Co., Ltd. (QS4FY-22003224).

References

- [1] G. Schmitt, et al., Global needs for knowledge dissemination, research, and development in materials deterioration and corrosion control, *World Corros. Organ.* 38 (2009) 14.
- [2] C.M. Hansson, The impact of corrosion on society, *Metall. Mater. Trans. A* 42 (10) (2011) 2952–2962.
- [3] Y. Shi, B. Yang, X. Xie, J. Brechtl, K.A. Dahmen, P.K. Liaw, Corrosion of Al_xCrFeNi high-entropy alloys: Al-content and potential scan-rate dependent pitting behavior, *Corros. Sci.* 119 (2017) 33–45.
- [4] H. Luo, Z. Li, A.M. Mingers, D. Raabe, Corrosion behavior of an equiatomic CoCrFeMnNi high-entropy alloy compared with 304 stainless steel in sulfuric acid solution, *Corros. Sci.* 134 (2018) 131–139.
- [5] C.-C. Yen, H.-N. Lu, M.-H. Tsai, B.-W. Wu, Y.-C. Lo, C.-C. Wang, S.-Y. Chang, S.-K. Yen, Corrosion mechanism of annealed equiatomic AlCoCrFeNi tri-phase high entropy alloy in 0.5 M H₂SO₄ aerated aqueous solution, *Corros. Sci.* 157 (2019) 462–471.
- [6] K. Yamanaka, H. Shiratori, M. Mori, K. Omura, T. Fujieda, K. Kuwabara, A. Chiba, Corrosion mechanism of an equimolar AlCoCrFeNi high-entropy alloy additively manufactured by electron beam melting, *npj Mater. Degrad.* 4 (2020) 24.
- [7] P. Cui, Z. Bao, Y. Liu, F. Zhou, Z. Lai, Y. Zhou, J. Zhu, Corrosion behavior and mechanism of dual phase Fe1.125Ni1.06CrAl high entropy alloy, *Corros. Sci.* 201 (2022) 110276.
- [8] C.P. Lee, C.C. Chang, Y.Y. Chen, J.W. Yeh, H.C. Shih, Effect of the aluminum content of AlxCrFe1.5MnNi0.5 high-entropy alloys on the corrosion behavior in aqueous environments, *Corros. Sci.* 50 (2008) 2053–2060.
- [9] Q. Zhao, Z. Pan, X. Wang, et al., Corrosion and passive behavior of AlxCrFeNi3-x (x= 0.6, 0.8, 1.0) eutectic high entropy alloys in chloride environment, *Corros. Sci.* 208 (2022) 110666.
- [10] A. Raza, S. Abdulahad, B. Kang, et al., Corrosion resistance of weight reduced AlxCrFeMoV high entropy alloys, *Appl. Surf. Sci.* 485 (2019) 368–374.
- [11] L. Feng, Y.D. Yuan, C.H. Bian, et al., Microstructure and properties of FeCrMnAlCu high-entropy alloy, *Mater. Sci. Technol.* 39 (10) (2023) 1245–1254.
- [12] M. Izadi, M. Soltanieh, S. Alamolhoda, et al., Microstructural characterization and corrosion behavior of AlxCrFeNi high entropy alloys, *Mater. Chem. Phys.* 273 (2021) 124937.
- [13] C.D. Taylor, P. Lu, J. Saal, G.S. Frankel, J.R. Scully, Integrated computational materials engineering of corrosion resistant alloys, *npj Mater. Degrad.* 2 (2018) 6.
- [14] Y. Shi, B. Yang, P.D. Rack, S. Guo, P.K. Liaw, Y. Zhao, High-throughput synthesis and corrosion behavior of sputter-deposited nanocrystalline Al_x(CoCrFeNi) 100-x combinatorial high-entropy alloys, *Mater. Des.* 195 (2020) 109018.
- [15] T. Barrès, B. Tribollet, O. Stephan, H. Montigaud, M. Boinet, Y. Cohen, Characterization of the porosity of silicon nitride thin layers by Electrochemical Impedance Spectroscopy, *Electrochim. Acta* 227 (2017) 1–6.
- [16] S.R. Allahkaram, M.H. Nazari, S. Mamaghani, et al., Characterization and corrosion behavior of electroless Ni-P/nano-SiC coating inside the CO₂ containing media in the presence of acetic acid, *Mater. Des.* 32 (2) (2011) 750–755.
- [17] S. Shuang, Z.Y. Ding, D. Chung, et al., Corrosion resistant nanostructured eutectic high entropy alloy, *Corros. Sci.* 164 (2020) 108315.
- [18] S. Marcellin, N. Pélisse, S. Regnier, Electrochemical characterisation of a martensitic stainless steel in neutral chloride solution, *Electrochim. Acta* 87 (2013) 32–40.
- [19] M.E. Orazem, B. Tribollet, V. Vivier, D.P. Riemer, E. White, A. Bunge, On the Use of the power-law model for interpreting constant-phase-element parameters, *J. Braz. Chem. Soc.* 25 (2014) 532–539.
- [20] D. Wallinder, J. Pan, C. Leygraf, A. Delblanc-Bauer, Eis and XPS study of surface modification of 316LVM stainless steel after passivation, *Corros. Sci.* 41 (1998) 275–289.
- [21] W. Wei, F. Mohammadi, A. Alfantazi, Corrosion behaviour of niobium in phosphate buffered saline solutions with different concentrations of bovine serum albumin, *Corros. Sci.* 57 (2012) 11–21.
- [22] H. Luo, S. Zou, Y.-H. Chen, Z. Li, C. Du, X. Li, Influence of carbon on the corrosion behaviour of interstitial equiatomic CoCrFeMnNi high-entropy alloys in a chlorinated concrete solution, *Corros. Sci.* 163 (2020) 108287.
- [23] C.B. Nascimento, U. Donatus, C.T. Rios, R.A. Antunes, Electronic properties of the passive films formed on CoCrFeNi and CoCrFeNiAl high entropy alloys in sodium chloride solution, *J. Mater. Res. Technol.* 9 (2020) 13879–13892.
- [24] K. Feng, Y. Zhang, Z. Li, C. Yao, L. Yao, C. Fan, Corrosion properties of laser cladded CrCoNi medium entropy alloy coating, *Surf. Coat. Technol.* 397 (2020) 126004.
- [25] G. Brug, A.L. van den Eeden, M. Sluyters-Rehbach, J.H. Sluyters, The analysis of electrode impedances complicated by the presence of a constant phase element, *J. Electroanal. Chem. Interfacial Electrochem.* 176 (1984) 275–295.
- [26] B. Song, Y. Hua, C. Zhou, Y. Li, L. Yang, Z. Song, Fabrication and anticorrosion behavior of a bi-phase TaNbHfZr/CoCrNi multilayer coating through magnetron sputtering, *Corros. Sci.* 196 (2022) 110020.
- [27] P. Varshney, R. Mishra, N. Kumar, Understanding the nature of passivation film formed during corrosion of Fe39Mn20Co20Cr15Si5Al1 high entropy alloy in 3.5 wt% NaCl solution, *J. Alloys Compd.* 904 (2022) 164100.
- [28] H. Luo, S. Zou, Y.H. Chen, et al., Influence of carbon on the corrosion behavior of interstitial equiatomic CoCrFeMnNi high-entropy alloys in a chlorinated concrete solution, *Corros. Sci.* 163 (2020) 108287.
- [29] H. Luo, Q. Yu, C. Dong, G. Sha, Z. Liu, J. Liang, L. Wang, G. Han, X. Li, Influence of the aging time on the microstructure and electrochemical behavior of a 15-5PH ultra-high strength stainless steel, *Corros. Sci.* 139 (2018) 185–196.

- [30] C. Liu, J. Wu, Influence of pH on the passivation behavior of 254SMO stainless steel in 3.5% NaCl solution, *Corros. Sci.* 49 (2007) 2198–2209.
- [31] J.W. Diggle, T.C. Downie, C. Goulding, Anodic oxide films on aluminum, *Chem. Rev.* 69 (1969) 365–405.
- [32] J. Soltis, Passivity breakdown, pit initiation and propagation of pits in metallic materials—review, *Corros. Sci.* 90 (2015) 5–22.
- [33] Y. Qiu, S. Thomas, M.A. Gibson, H.L. Fraser, K. Pohl, N. Birbilis, Microstructure and corrosion properties of the low-density single-phase compositionally complex alloy AlTiCr, *Corros. Sci.* 133 (2018) 386–396.
- [34] M.H. Dean, U. Stimming, The electronic properties of disordered passive films, *Corros. Sci.* 29 (1989) 199–211.
- [35] J.L. LV, H.J. Jin, Corrosion resistance mechanism of the passive films formed on ascast FeCoCrNiMn high-entropy alloy, *Mater. Res. Express* 7 (2020).
- [36] G.A. Zhang, Y.F. Cheng, Micro-electrochemical characterization and Mott–Schottky analysis of corrosion of welded X70 pipeline steel in carbonate/bicarbonate solution, *Electrochim. Acta* 55 (1) (2009) 316–324.
- [37] A. Fattah-Alhosseini, F. Soltani, F. Shirzalimi, et al., The semiconducting properties of passive films formed on AISI 316 L and AISI 321 stainless steels: A test of the point defect model (PDM), *Corros. Sci.* 53 (10) (2011) 3186–3192.
- [38] D.D. Macdonald, The point defect model for the passive state, *J. Electrochem. Soc.* 139 (1992) 3434.
- [39] D.D. Macdonald, The history of the point defect model for the passive state: a brief review of film growth aspects, *Electrochim. Acta* 56 (2011) 1761–1772.
- [40] C. Chao, L. Lin, D. Macdonald, A point defect model for anodic passive films: I. Film growth kinetics, *J. Electrochem. Soc.* 128 (1981) 1187.